Resonant Bragg scatter of surface plasmons on nanohole arrays

2006 New J. Phys. 8 57

(http://iopscience.iop.org/1367-2630/8/4/057)

New Journal of Physics
The open-access journal for physics

Resonant Bragg scatter of surface plasmons on nanohole arrays

E Altewischer, X Ma, M P van Exter and J P Woerdman
Huygens Laboratory, Leiden University, PO Box 9504, 2300 RA Leiden, The Netherlands
E-mail: mvexter@molphys.leidenuniv.nl

New Journal of Physics **8** (2006) 57
Received 4 October 2005
Published 19 April 2006
Online at http://www.njp.org/
doi:10.1088/1367-2630/8/4/057

Abstract. Using microscopic imaging, we study the generation and propagation of beams of surface plasmons (SPs) on a hexagonal metal nanohole array. We discuss the wavelength-dependent propagation, a Fano-type interference and the possibility to generate focused SP beams. Prominent forking of these beams is attributed to resonant (Bragg) scattering from consecutive lattice planes. This claim is supported by a coupled-mode model.

Contents

PII: S1367-2630(06)09446-8

1. Introduction

The field of metal nano-optics has attracted lots of interest lately. This interest has been inspired by observations of enhanced transmission of nanohole arrays [1], as well as the possibilities for performing two-dimensional (2D) optics with surface plasmons (SPs) [2] and the potential of miniaturization to subwavelength dimensions. Recent experiments have shown that it is relatively easy to excite SPs locally and follow their propagation along a metal interface. While the finest subwavelength details can be observed only with scanning near-field optical microscopy (SNOM) [3]–[5], a simple microscopic imaging system is sufficient to observe the long-range propagation, damping and interference of the SPs [6, 7]. In some aspects this 'far-field' imaging system is even superior to the SNOM system, because it has a larger dynamic range, is much easier to operate and presents much less ambiguity in interpretation.

In this paper, we use microscopic imaging to observe the propagation of directional beams of SPs generated by local excitation on a hexagonal nanohole array. The exceptionally large propagation length of the SPs on this hexagonal array (see section 2) allows us to visualize interesting physics that remains hidden on arrays with smaller SP propagation. We demonstrate and discuss the wavelength dependence of the SP propagation, in particular the relation between the excited SP beams and the SP bandstructure of the hole array. We also discuss briefly the Fano-type interference between two transmission channels [7]–[9], being the non-resonant direct transmission through the holes and the resonant excitation and subsequent decay of SPs. Additionally, we show that the SP beams are coherent and can display a focus as they propagate along the array. The position-resolved experiments we present here are complementary to previously reported angle-resolved transmission measurements [10].

The dynamics of SPs on nanohole arrays can be quite different from those observed on smooth metal films. The additional scattering by the holes leads to increased damping and (small) changes of the SP propagation speed. These effects are expected to be most prominent around Brillouin zone boundaries, where scattering at consecutive Bragg planes interferes constructively. The resulting coupling between the travelling SP waves can give the SP eigenmodes a standing-wave character and lead to a pronounced bending of the SP dispersion curve away from the relation [11]

$$|\vec{k}_{\mathrm{SP}}| = \sqrt{\frac{\epsilon_d \epsilon_m}{\epsilon_d + \epsilon_m}} \frac{\omega_{\mathrm{SP}}}{c}, \tag{1}$$

where ϵ_m and ϵ_d are the dielectric functions of the metal and dielectric and $\vec{k}_{\mathrm{SP}}$ and ω_{SP} are the SP momentum and frequency, respectively. This relation is commonly used to describe SPs on hole arrays, although it applies strictly speaking only to a smooth interface. In this paper, we demonstrate how band bending and the associated changes in the SP group velocity can considerably modify equation (1) and change the spatial structure of the generated SP beams.

Band effects in 2D periodic systems have recently been discussed in several other papers. Ropers *et al* [12] have mapped the transmission amplitude and phase of a metal hole array under various angles, calculated the dispersion diagram and emphasized the differences between the radiating and non-radiating modes. Hibbins *et al* [13] have used a related angle-resolved technique in reflection to determine the dispersion characteristics of designer SPs at microwave frequencies. Giannattasio and Barnes [14] have directly visualized the wavevector dispersion of SP modes on a grating by exciting SPs through surface roughness followed by angular-resolved imaging.

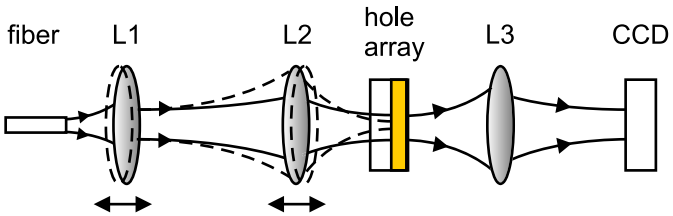

Figure 1. Experimental setup in which the hole array, positioned with its glass side oriented towards the input beam, is illuminated with a tightly focused beam. The position-resolved transmission is obtained through direct imaging on to a CCD. The dashed curves indicate an input beam that is focused tighter on the array by displacing objectives L1 and L2 with respect to their positions corresponding to the solid lines.

2. Experimental setup

Our nanohole array was fabricated with focused ion beam milling and consisted of a 200 nm thick gold film on a 0.5 mm thick glass plate with a 2 nm thick titanium bonding layer in between. The holes of 180 nm diameter were spaced in a hexagonal lattice with lattice period $a = 883$ nm. When illuminated by a beam with a small opening angle, the array shows a transmission peak at a wavelength of 807 nm that corresponds to the first-order SP mode at the air–metal interface at $k_{SP} = 4\pi/(\sqrt{3}\,a)$ (see [10] for an SEM picture and a transmission spectrum).

Figure 1 shows the optical beam line, which starts with a frequency-tunable cw laser beam that is mode-cleaned by a single-mode fibre. Two microscope objectives allow us to adjust the size of the focus on the hole array, which is positioned with its glass side towards the beam. The accessible range of beam waists in the focus is from 1.2 to $\approx$20 μm (half width at e^{-2} intensity point). A third objective projects an 80$\times$ magnified image of the backside of the array on to a CCD. To minimize (spherical) aberrations great care was taken in selecting the illumination objective L2 (40$\times$, NA = 0.6 with adjustable glass correction) and the imaging objective L3 (50$\times$, NA = 0.6), both with long working distance. With this setup, we could resolve structures of around 1.0 μm.

The most important limitation of the imaging technique arises from reflections from the imaging objective. This generates interference between the light transmitted through the array and an enlarged back-reflected version thereof, which sets a limit to the signal-to-noise ratio. Nevertheless, a dynamic range of more than four orders of magnitude was achieved in the measurements.

3. Analysis of SP propagation

The spatially resolved transmission of our hexagonal array is shown in figure 2 for an input wavelength of (a) 750, (b) 800, (c) 807 and (d) 830 nm. In this measurement, the array was positioned at the focus of a Gaussian illumination beam with 1.6 μm-waist (half width at e^{-2} intensity point) that was linearly polarized along the direction indicated by the double-headed arrow in the figure. To increase the signal-to-noise ratio and remove the speckle pattern observed in single images, the images were averaged over 100 different illumination positions, where care

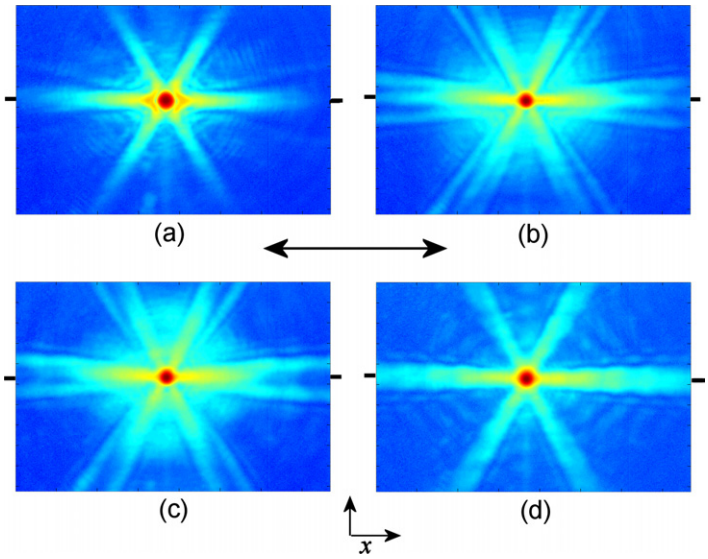

Figure 2. Transmission images of the hole array, illuminated with a laser beam of 1.6 μm width at a wavelength of (a) 750, (b) 800, (c) 807 and (d) 830 nm. The colours indicates the transmission intensity on a logarithmic scale. The pictures are 57 $\times$ 85 μm full scale.

was taken to stay far enough from the array edges. In each of the images of figure 2, the overall structure is the same: it comprises a bright central spot and six SP beams oriented at angles of 0°, 60°, . . . , 300°, the 0° and 180° beams being about four times as bright as the other four beams. On a more detailed level however there are important differences, such as the intensity dips in the horizontal SP beams alongside the central spot in the 750 nm picture and, as most prominent feature, a splitting of each SP beam into two or three 'forks' at 800 and 807 nm. This 'forking' of the SP beams will be discussed in more detail in sections 4 and 5. Note, that although the transmission spectrum for plane-wave illumination at normal incidence contains only a rather narrow resonance (FWHM $\approx$ 20 nm) around 807 nm [15], the excitation of SP beams is now even possible at 750 and 830 nm because of the spectral broadening of the SP resonance induced by the focused excitation.

Figure 3 shows normalized cross-sections of the transmission profiles along the (horizontal) directions in between the black markers in figure 2. Consecutive cross-sections are shifted by factors of 10. Additionally, the (green) curve at the bottom of figure 3 is a cross-section of the input Gaussian beam. All cross-sections clearly show two contributions: (i) a 'direct transmission' which is practically identical to the Gaussian input beam in the centre, and (ii) 'wings' that decay more or less exponentially away from the centre. These two contributions have also been observed for a square nanohole array [5, 15]. The central contribution results from light leaking directly through the subwavelength holes, whereas the wings are due to resonant excitation of SPs that propagate on the array. At positions where the contributions are of equal order of magnitude they interfere most prominently. For a wavelength of 750 nm, i.e., smaller than the resonance wavelength, the destructive interference is best visible, generating the dips in the spatial profiles around the central peak in figure 3. This observation is consistent with simulations similar to those reported in [15].

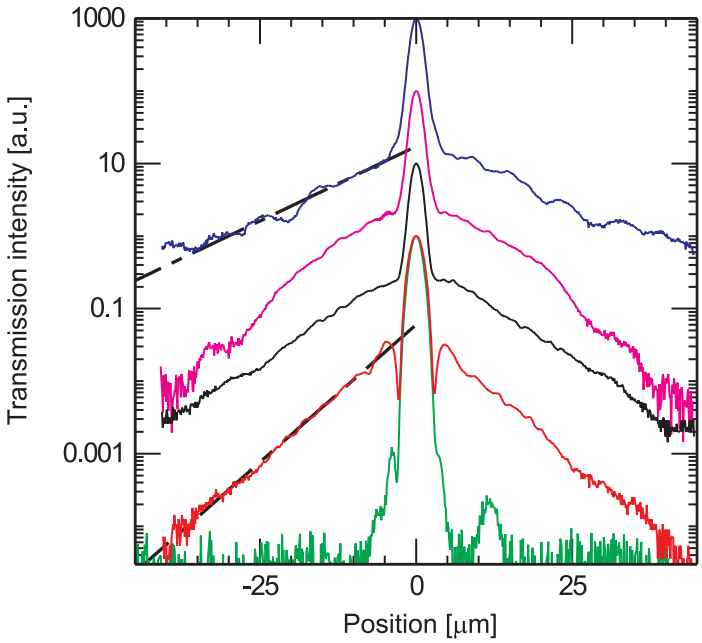

Figure 3. Cross-sections of transmission images cut along lines through the black markers in figure 2, for illumination with a laser beam of width 1.6 μm at a wavelength of, from bottom to top, 750, 800, 807 and 830 nm. The lowest curve (green) is the illumination beam transmitted through bare glass. Note that the dynamic range is more than four orders of magnitude.

The peak intensity of the direct transmission is stronger than that of the wings at all observed wavelengths in figure 3. This is because the SP-assisted contribution in the wings is spread out over a much larger area than the central direct contribution, which just mimics the pump profile. After spatial integration, the SP contribution does dominate, as was also observed in the transmission spectrum of the hole array under 'plane-wave' illumination [7]. The direct transmission was experimentally found to be largest at the smallest wavelength, which is in agreement with the theoretical Rayleigh-like transmission of a subwavelength aperture [16]. The transmission of the central peak is about 0.4% at 807 nm, being an order of magnitude smaller than the 4% peak transmission observed for plane-wave illumination at normal incidence because of the spectral broadening due to focused excitation.

The decaying wings in figure 3 are generally well fit by exponentials such as the two dashed lines. These fits give SP propagation lengths of $5.9 \pm 0.6\,\mu$m for a wavelength of 750 nm, $7.6 \pm 0.6\,\mu$m ($\lambda = 800$ nm), 7.9 or 4.3 μm ($\lambda = 807$ nm; see next section) and $11.0 \pm 1.5\,\mu$m ($\lambda = 830$ nm). The clear increase in the propagation length for increasing wavelength is in agreement with the decreased scatter efficiency of the holes and (to a lesser extent) the reduced intrinsic damping of the metal. The measured propagation lengths are exceptionally large in comparison to values of around 2 μm measured for similar square arrays [4, 7]. We attribute this difference to three effects: (i) we deal with SPs at a metal–air instead of a metal–glass interface, (ii) the holes are relatively small (only $\approx$180 μm diameter) and (iii) the excited SPs travel approximately along bisectors of the real-space lattice and might thereby experience somewhat less scatter.

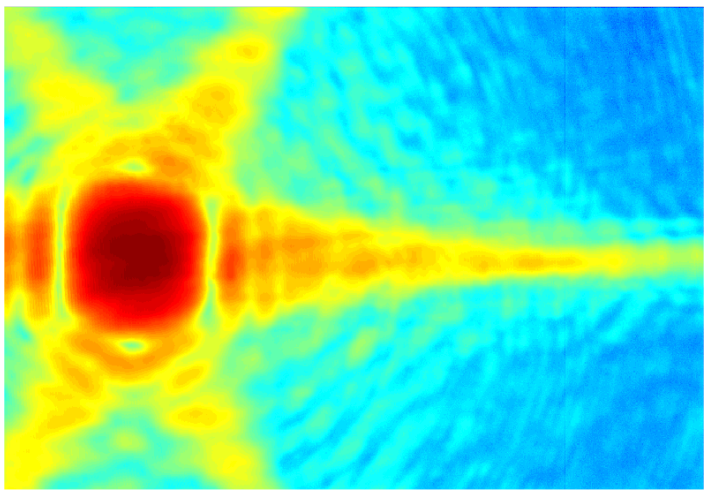

Figure 4. Focused SP beams appear in the transmission image upon defocusing of the lens L2 in the setup of figure 1, at an input wavelength of 830 nm. The colour scale is based on logarithmic intensities, with yellow at 10^{-2} and dark blue at 10^{-4} of the red peak. The picture is $57 \times 85\ \mu$m full scale.

Figure 4 presents an interesting demonstration of the coherence properties of the SP beams on the hole array. In this measurement, the illuminating objective L2 is displaced towards the array (in comparison with the earlier measurement) to create a converging optical beam at the array, whereas the imaging objective is not moved. The wavelength was set to 830 nm to optimize the SP propagation length. The SP beams generated in the plane of the array are clearly focused as they propagate in this plane. In the measurement of figure 4, the objective L2 was displaced by $50 \pm 5\ \mu$m, which generated SP beams that narrowed down from a width of $12\ \mu$m in the centre to $2.2\ \mu$m in the focus. The distance from the centre of the illumination beam to the position of the focus was measured as $55 \pm 10\ \mu$m. In a different experiment with less defocusing of objective L2, we observed that the SP beam diverged again after the focus and produced shapes similar to those in figure 2.

Figure 4 contains a lot of detailed structure, such as intensity oscillations in the SP beams with a period of 5–10 μm and intriguing ripples in between the SP beams. We attribute these oscillations and ripples to interference effects, the details of which are not yet completely understood. We have also observed faster oscillations on a length scale of 1.5–2.0 μm that disappear after averaging over illumination positions. A possible explanation for these fast oscillations is the beating of SP waves travelling at different speeds on the front and back sides of the hole array (glass versus air) [3].

Our imaging method also allows us to measure the 'free' SP propagation on the smooth gold film adjacent to the hole array. By illuminating the array at a position near one of its edges, the excited SPs travelling in the direction of the edge are 'launched' out of the array into the smooth film. An analysis of the resulting exponential decay of the propagating SPs gives a propagation length of 19 μm for 807 nm wavelength illumination. This is a factor of 2 smaller than the value of 40 μm calculated for a perfectly smooth gold film [17]. We attribute this difference to surface roughness. The fact that we see the SPs propagate on the bulk gold, albeit with only a few per

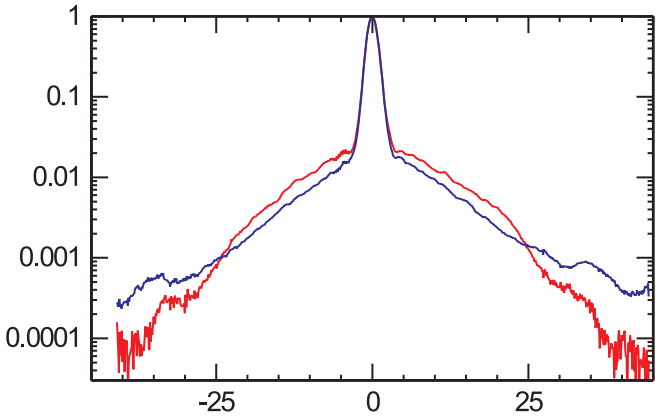

Figure 5. Cross-sections along the central horizontal SP beams (red curve) and along the forks (blue curve), for illumination with a laser beam of width 1.6 μm at a wavelength of 807 nm.

cent of the scattered intensity that they have on the hole array, already shows that there is at least sufficient roughness to scatter from even on a non-patterned 'smooth' film.

As an aside, we note that an SP beam propagating at an angle with respect to the edge of the hole array is expected to experience a small deflection upon entering the bulk gold, due to the difference in propagation speeds in these two 'media'. This effect was indeed observed, albeit with modest accuracy; using Snell's law we calculate the ratio of the effective refractive indices as $n_1/n_2 = 1.04 \pm 0.02$.

Most of the experiments were repeated with a larger illumination spot of 3.4 μm waist, made by moving both lenses L1 and L2 in figure 1. Compared to the previously discussed measurements, the peak intensity is now lower but the SP beam intensity is larger. The first observation is caused by the 'dilution' of the input power due to the larger waist, the second observation is caused by the higher SP excitation efficiency of a beam with a smaller spread in transverse momentum. The observed SP decay was found to be the same, being largest at long wavelengths and non-exponential around 807 nm.

4. Forks due to Bragg reflection

A closer examination of the spatial images of figure 2 shows that the SP beams are split into two or three parts for wavelengths around 807 nm. To illustrate this, figure 5 shows transmission cross-sections for illumination at 807 nm along (i) the bisector of the two forks, i.e. the central SP beam axis and (ii) lines oriented along the centre of one of the fork arms themselves. The decay along the fork arms is nicely exponential, with an associated SP propagation length of 7.9 μm. The decay along the central cut is quite different and seems to consist of two differently decaying parts that have a rather abrupt transition: the first part has a decay length of 8.0 μm and the second has a decay length of 4.3 μm. This non-exponential decay is typical for the dark regions in between forks.

If the wavelength of the illumination is varied around 807 nm, the number of fork arms per SP beam, their opening angle and relative angles change. For instance, at 807 nm, there are two

prominent forks, oriented at +6° and −6° with respect to the central SP beam axis, whereas at 800 nm there are three prominent fork arms, where the two outer ones make an angle of ±7.5° with respect to the central one. If the wavelength is detuned sufficiently from 807 nm, the forks disappear. This indicates that the forks are caused by a resonance effect that occurs when the excited SP wavevector approaches a Brillouin zone boundary, being in this case a folded zone at reduced momentum $k_{\parallel} = 0$. This can be explained in two ways that are 'equivalent': in the spatial and in the Fourier domain. In the spatial domain, it is the interference from scattering of the SP waves at holes in consecutive lattice planes that slows down their propagation. In the Fourier domain, it is the band-bending of the dispersion relation $\omega_{\mathrm{SP}}(k_{\parallel})$ that reduces the SP group velocity $v_{\mathrm{gr}} = \partial\omega/\partial k_{\parallel}$ and thereby reduces their propagation distance even if their lifetime would remain unchanged. The directional dependence of the SP dispersion can via this mechanism yield a fork-like pattern, as we will show in the next section.

5. Model based on six coupled SP waves

In this section, we will explain the observed fork-like patterns with a model that is based on the dynamics of the six fundamental SP modes in the hexagonal array and their coupling to the input and output optical field. Central in this description is the notion that the SP dynamics on a hole array can be quite different than that on a smooth metal film due to the scattering at the holes. Furthermore, our 'plasmonic crystal' is more complicated than either the well-known non-absorbing photonic crystals [18] or the periodic structures found in any solid-state textbook [19]. The first (and most important) complication is that we are not dealing with a solitary system, but that we instead probe our 2D plasmonic crystal only via its coupling to free photons in the third dimension. As this coupling occurs only at the holes, we preferentially excite and detect the cosine-type standing waves, having anti-nodes at the holes. A second reason why our system is non-standard is that the SP dynamics is damped. The mentioned preferential excitation even makes the damping mode-specific and leads to 'dissipative coupling' between the SP travelling waves, being the same type of coupling that can lock the travelling waves in a optical gyroscope [20]. As a third point, we note that the coupling between SPs and photons is not only mode specific, but also polarization-dependent. For these three reasons, we will discuss our model in quite some detail.

The most important simplification in our model is the assumption that the transmission is only carried by SPs on a single interface of the asymmetric metal film. This is a reasonable starting point, because under our experimental conditions the six fundamental SP modes on the metal–air interface are resonantly excited, whereas the SP modes on the metal–glass interface are far off-resonance. For any incident optical plane wave with projected photon momentum $\vec{k}_{\parallel}$, we can thus approximately write the combined plasmon field as the sum over six travelling SP modes having momenta $\vec{k}_{\mathrm{SP}} = \vec{k}_{\parallel} + \vec{G}_i$, where the fundamental lattice momenta $\vec{G}_j = 4\pi/(\sqrt{3}\,a)\,\vec{e}_j$, where $\vec{e}_j$ is the unit vector along $\varphi_j = \{0°,\ 60°,\ 120°, \ldots,\ 300°\}$ and a is the spacing in the hexagonal lattice. To describe the joint evolution of these six SP waves, we extend the two-mode model of Ropers *et al* [12] to a more elaborate six-mode model:

$$\frac{\mathrm{d}}{\mathrm{d}t}\vec{u} = -\mathrm{i}\,(\mathcal{H} + V - \mathrm{i}\Gamma)\,\vec{u}, \tag{2}$$

where $\vec{u}$ comprises the six modal amplitudes, $\mathcal{H}$ describes the natural evolution of the uncoupled SP waves, $\mathcal{V}$ contains the energy-conserving interaction from SP scatter at the holes and Γ is the damping matrix that also contains the dissipative coupling.

The evolution matrix $\mathcal{H}$ is diagonal in the travelling-wave basis (electric fields proportional to $\exp(\mathrm{i}\vec{k}_{\mathrm{SP}} \cdot \vec{r})$) via $\mathcal{H} = \mathrm{diag}(\omega_1, \omega_2, \ldots, \omega_6)$, as the eigenfrequencies ω_j of travelling SP waves on a smooth metal–dielectric interface depend only on their momentum $\vec{k}_{\parallel} + \vec{G}_i$ (see equation (1)).

The interaction matrix $\mathcal{V}$ describes the energy-conserving scatter from each of the six SP travelling wave into the others. We think that a realistic model for this scatter can be obtained by assuming that the holes are small enough to act as simple dipole scatterers. The polarization aspect makes the effective potential slightly more complicated than the muffin-tin potential in solid-state physics [19]. We distinguish between two different orientations of the mentioned dipoles: they are either oriented along the surface normal, and parameterized by amplitude s, or oriented in the surface plane along the SP propagation direction, and parameterized by amplitude p. The s-scatter is isotropic, whereas the p-scatter has the familiar anisotropic dipolar shape that results from the in-plane polarization projection. In the travelling-wave basis, the elements of the scatter matrix thus become $\mathcal{V}_{ij} = s + p\,\cos(\varphi_i - \varphi_j)$. For very small holes, we expect the in-plane dipole to be much smaller than the out-of-plane dipole, making $p \ll s$.

The damping matrix Γ is most simple in the standing-wave basis (electric fields of counter-propagating SPs are combined into standing waves), where, in the small-hole approximation, we only need to distinguish between the cosine and the sine modes. The sine waves have nodes at the holes and thus experience only the intrinsic damping rate Γ_m caused by the Ohmic losses in the metal. The cosine waves have antinodes at the holes and thus experience additional losses due to scatter of SPs into light, at an extra radiative damping rate Γ_r [12].

We observe the SP dynamics in the hole array only through its coupling to the optical field in the third dimension. In our calculation of the optical transmission profile, we neglect the direct transmission, which is visible only in the central pump region, decompose the incident optical field into its plane-wave components, and calculate the transmission of each plane-wave component. The array symmetry and limited opening angle of our imaging system, allows us to write the input–output relation of each of these plane-wave components as $\vec{E}_{\mathrm{out}}(\vec{k}_{\parallel}, \omega) = t(\vec{k}_{\parallel}, \omega)\vec{E}_{\mathrm{in}}(\vec{k}_{\parallel}, \omega)$, where $t(\vec{k}_{\parallel}, \omega)$ is the complex transmission amplitude at the in-plane wavevector component $\vec{k}_{\parallel}$ and frequency ω[10]. A Fourier transformation of the input–output relation at fixed ω shows that the spatial output profile $\vec{E}_{\mathrm{out}}(\vec{x}, \omega)$ is just a convolution of the input profile $\vec{E}_{\mathrm{in}}(\vec{x}, \omega)$ with a 'point spread function' $\tilde{t}(\vec{x}, \omega)$ that is the Fourier transform of $t(\vec{k}_{\parallel}, \omega)$.

Before discussing the parameters and results of the six-mode model, we will take one step back and try to demonstrate the essential physics in a simplified version of the model. We will use a 1D description and consider only two travelling SP waves, with momenta $k_{\parallel} + G$ and $k_{\parallel} - G$ around $k_{\parallel} = 0$. The dispersion that these waves would have on a smooth metal surface (equation (1)) is depicted by the two sloping dashed lines in figure 6. The energy-conserving scatter at the holes produces a coupling between the travelling SP waves that translates into an avoided or Landau–Zener crossing of the energy levels, as depicted by the solid hyperbolic-shaped curves in figure 6. At $k_{\parallel} = 0$, the two eigenmodes are pure standing waves with either a cosine or sine field pattern, whereas going away from normal incidence ($k_{\parallel} \neq 0$) more and more travelling-wave character is mixed in. The cosine mode has anti-nodes at the holes and is strongly coupled to the photon field; the sine mode has nodes and is basically invisible (non-radiative) [12].

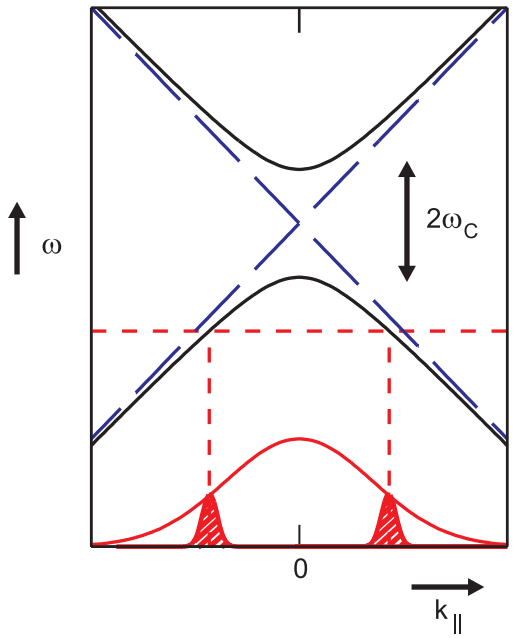

Figure 6. This 1D cut of the SP bandstructure in a folded-zone representation shows the almost straight dispersion of two uncoupled SP modes (dashed curves) and the avoided-crossing of the coupled SP modes (solid curves). Upon excitation with a monochromatic focused beam, the hole array selects specific momenta $k_{\|}$ out of the applied broad distribution (bottom curves and short-dashed lines).

Next we consider an incident monochromatic wave at frequency ω that is focused relatively tightly on to the array and thereby provides a large range of available momenta $k_{\|}$, as depicted by the broad Gaussian curve at the bottom of figure 6. The intersections between the horizontal dashed line at frequency ω and the solid SP dispersion curve determines the resonant values $k_{\|} = \pm k_0$ that are selected out of the incident field and are allowed to propagate as SP waves. The momentum bandwidth in this selection (depicted by the two sharp curves) is Fourier-related to the propagation distance of the excited SPs in real space. The crucial point now is that this propagation distance is determined both by the SP life time as well as their group velocity. If the local derivative $v_{\mathrm{gr}} = \mathrm{d}\omega/\mathrm{d}k_{\|}$ is small then SP propagation length is small as well. Around $k_{\|} = 0$ the group velocity v_{gr} even goes to zero and the SPs are stopped in their tracks.

In the 1D presentation of figure 6, excitation of SPs with optical frequencies inside the bandgap is not possible. Real SPs can, however, also have momentum k_y perpendicular to the chosen 1D projection, and the SP dispersion curves of figure 6 should be extended with a third dimension. The avoided crossing in the planar representation of figure 6 now becomes a saddle-like 3D structure. Thus, for frequencies that are within the bandgap of the 1D model resonant $\vec{k}_{\|}$ values can still be found in the 2D model, albeit at $k_y \neq 0$. Out of the focused input beam that among others excites divergent SP beams in the approximate k_x direction, the array will select only those (relatively small) nonzero k_y components for which SPs really exist and propagate. Therefore, we attribute the experimentally observed forks to the preferential excitation and propagation of such $k_y \neq 0$ SP waves.

After this small detour, we return to our six-mode model. The procedure that we use to calculate the amplitude transmission function $t(\vec{k}_{\|}, \omega)$ of our hexagonal array is as follows: for

an incident cw plane-wave optical field, we solve the dynamics of the six relevant SP modes $\vec{k}_\parallel + \vec{G}_j$ by replacing the time-evolution $\mathrm{d}/\mathrm{d}t$ in equation (2) by $-\mathrm{i}\omega$. The incident optical field is projected on to the SP waves by adding an extra term $\vec{u}_{\mathrm{in}} = E_{\mathrm{in}}\vec{e}_{\mathrm{project}}$ to the right-hand side of equation (2). Finally, the six SP amplitudes in $\vec{u}$ are calculated and projected back into an output optical field via $E_{\mathrm{out}} = \vec{e}_{\mathrm{project}} \cdot \vec{u}$. The six-element vector $\vec{e}_{\mathrm{project}}$ contains both modal and polarization aspects; if the incident light is linearly polarized at an angle φ, the jth element of the projection vector is $(\vec{e}_{\mathrm{project}})_j = \cos(\varphi_j - \varphi)$. After these modal and polarization projections, the 6×6 matrix formalism reduces to the single transmission function $t(\vec{k}_\parallel, \omega)$. A 2D Fourier transform finally yields the spatial response function $\tilde{t}(\vec{x}, \omega)$. All calculations are performed in Mathematica.

To compare our simulations with the experimental data, we have normalized the projected momentum $\vec{k}_\parallel$ to the fundamental lattice momentum $|\vec{G}_j|$ and all frequencies and rates to the corresponding frequency ω_0 of SPs on a smooth, loss-free metal. We have not made any serious effort to optimize all parameters, because we realize that our model has a limited validity, in particular because it describes only the SP dynamics on the resonant interface. However, we do claim that the six-mode model produces the observed physics for reasonable parameters. These parameters were chosen as follows: from the observed damping lengths of the travelling SP waves in the metal and in the hole array far from resonance, we estimate the normalized damping rates as $\Gamma_m/\omega_0 = 0.003$ and $\Gamma_r/\omega_0 = 0.01$. From the angle-dependent transmission spectra observed in earlier experiments [21], we estimate the bandgap as $|6s + 3p| \approx 0.03$, where the bandgap formula $|6p + 3s|$ follows from the eigenvalues of the operator in the right-hand side of equation (2). In the small-hole approximation, we can neglect the in-plane dipole scatter and take $p/\omega_0 = 0$, and consequently $s/\omega_0 = -0.005$.

A cross-section of the calculated intensity transmission $|t(\vec{k}_\parallel, \omega)|^2$ in the $k_y = 0$ plane is shown in figure 7. The upper and lower bands are dominantly x-polarized and are the 'non-radiative (sine-like)' and 'radiative (cosine-like)' SP modes. The intermediate bands are twofold degenerate and dominantly polarized at $\pm 60^\circ$. The bandgap around $\omega = \omega_0$ and $k = 0$ is just visible. Figure 8 shows the corresponding spatial response function for a Gaussian input beam with the same waist as in the experiment (2.1 units of $a\sqrt{3}/2 = 1.6\,\mu\mathrm{m}$) at a frequency of $0.96\,\omega_0$. The picture shows a good qualitative agreement with the experimental results and, most importantly, the forks are clearly reproduced. When the frequency of the input field is changed the forks in the calculations also change shape and disappear far from resonance. The spatial profiles calculated theoretically show a surprisingly large variation with the input parameters.

6. Concluding discussion

We have discussed a simple experimental method to image the propagation of SPs on hole arrays directly. Using this method, the SP propagation length, and from that information about the SP bandstructure, can be obtained. In the observed spatial profiles, a Fano-type interference between a resonant SP contribution and a non-resonant direct contribution was observed. We have also shown that it is possible to shape the SP beams on the hole array by defocusing the input optical beam.

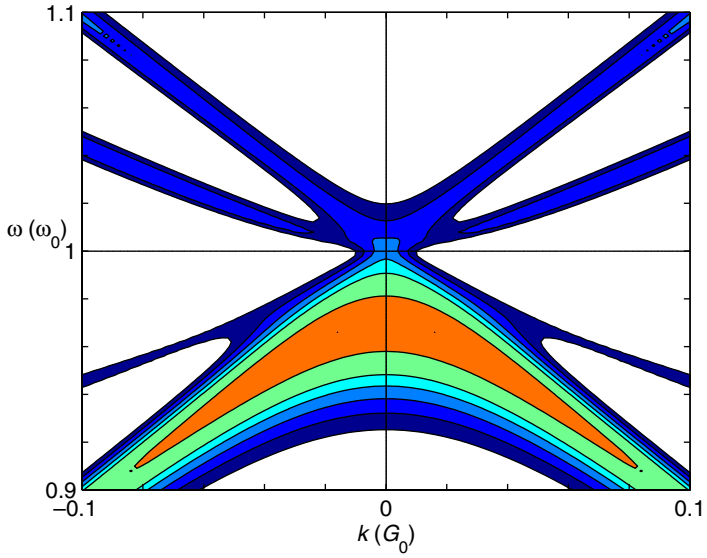

Figure 7. Simulation of the transmission intensity as a function of the parallel momentum $k_{\|}$ and frequency ω. The upper and lower SP bands have a width determined by the cosine- and sine-mode damping and show an avoided-crossing around $\omega = \omega_0$. Both intermediate bands are twofold degenerate, bringing the total number of bands to six. These bands are weaker because they are dominated by SP waves with $\pm 60^{\circ}$ polarization. The colours indicate the transmission intensity on a logarithmic scale, where each colour spans approximately a factor 1.35. The lower band provides by far the largest transmission.

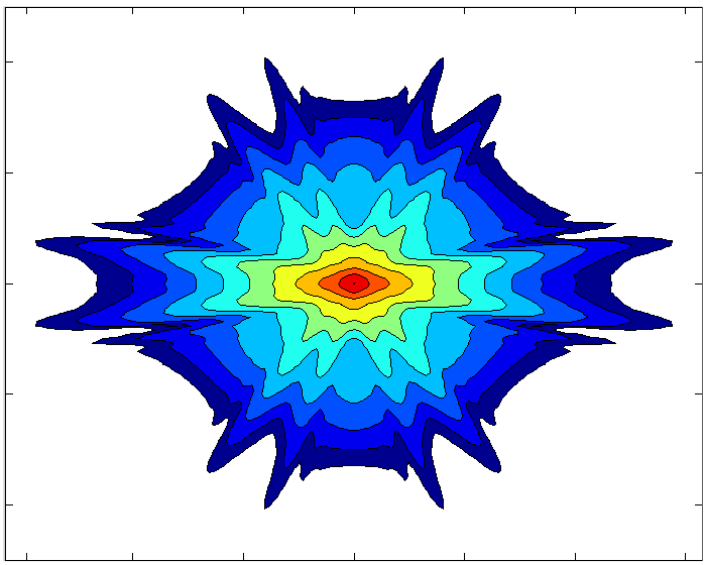

Figure 8. Simulation of the forks. The transmission intensity in the transverse plane is indicated using a logarithmic colour scale, where each colour spans a factor 3. The tick marks are placed at 20 μm intervals.

The most interesting feature of the experimental images is the occurrence of forks in the SP beams for frequencies near the plane-wave illumination resonance. We have used a simple model to relate these forks to bandgap effects that arise from scattering-induced coupling between different SP waves. The model reproduces the experimental features qualitatively, but falls short on a detailed level. The most important addition to the model that we think would be necessary to improve the fit to measurements is the inclusion of the second metal–dielectric interface and the coupling between the two interfaces.

Acknowledgments

This work is part of the research program of the Stichting voor Fundamenteel Onderzoek der Materie (FOM). We thank P F A Alkemade at the Kavli Institute for Nanoscience, Delft, The Netherlands, for producing the hole array sample.

References

[1] Ebbessen T W, Lezec H J, Ghaemi H F, Thio T and Wolff P A 1998 Extraordinary optical transmission through sub-wavelength hole arrays *Nature* **391** 667

[2] Ditlbacher H, Krenn J R, Schider G, Leitner A and Aussennegg F R 2002 Two-dimensional optics with surface plasmon polaritons *Appl. Phys. Lett.* **81** 1762

[3] Seidel J, Baida F I, Bisschoff L, Guizal B, Grafström S, van Labeke D and Eng L M 2004 Coupling between surface plasmon modes on metal films *Phys. Rev.* B **69** 121405

[4] Kim D S, Hohng S C, Malyarchuk V, Yoon Y C, Ahn Y H, Yee K J, Park J W, Kim J, Park Q H and Lienau C 2003 Microscopic origin of surface-plasmon radiation in plasmonic band-gap nanostructures *Phys. Rev. Lett.* **91** 143901

[5] Egorov D, Dennis B S, Blumberg G and Haftel M I 2004 Two-dimensional control of surface plasmons and directional beaming from arrays of subwavelength apertures *Phys. Rev.* B **70** 033404

[6] Tetz K A, Rokitski R, Nezhad M and Fainman Y 2005 Excitation and direct imaging of surface plasmon polariton modes in a two-dimensional grating *Appl. Phys. Lett.* **86** 111110

[7] Altewischer E, van Exter M P and Woerdman J P 2005 Fano-type interference in the point-spread function of nanohole arrays *Opt. Lett.* **30** 2436

[8] Genet C, van Exter M P and Woerdman J P 2003 Fano-type interpretation of red shifts and red tails in hole array transmission spectra *Opt. Commun.* **225** 331–6

[9] Sarrazin M, Vigneron J-P and Vigoureux J-M 2003 Role of Wood anomalies in optical properties of thin metallic films with a bidimensional array of subwavelength holes *Phys. Rev.* B **67** 085415

[10] Altewischer E, van Exter M P and Woerdman J P 2003 Polarization analysis of propagating surface plasmons in a subwavelength hole array *J. Opt. Soc. Am.* B **20** 1927–31

[11] Ghaemi H F, Thio T, Grupp D E, Ebbesen T W and Lezec H J 1998 Surface plasmons enhance optical transmission through subwavelength holes *Phys. Rev.* B **58** 6779–82

[12] Ropers C, Park D J, Stibenz G, Steinmeyer G, Kim J, Kim D S and Lienau C 2005 Femtosecond light transmission and subradiant damping in plasmonic crystals *Phys. Rev. Lett.* **94** 113901

[13] Hibbins A P, Evans B R and Sambles J R 2005 Experimental verification of designer surface plasmons *Science* **308** 670–2

[14] Giannattasio A and Barnes W L 2005 Direct observation of surface plasmon-polariton dispersion *Opt. Exp.* **13**

[15] Altewischer E, van Exter M P and Woerdman J P 2005 Analytic model of optical depolarization in square and hexagonal nanohole arrays *J. Opt. Soc. Am.* B **22** 1731
[16] Bethe H A 1944 Theory of diffraction by small holes *Phys. Rev.* **66** 163–82
[17] Raether H 1988 *Surface Plasmons* (Berlin: Springer)
[18] Soukoulis C M 1996 *Photonic Band Gap Materials* (Dordrecht: Kluwer)
[19] Kittel C 1971 *Introduction to Solid State Physics* (New York: Wiley)
[20] Chow W W, Gea-Banacloche J, Pedrotti L M, Sanders V E, Schleich W and Scully M O 1985 The ring laser gyro *Rev. Mod. Phys.* **57** 61
[21] Altewischer E 2005 Sub-wavelength hole arrays, surface plasmons and quantum entanglement *PhD Thesis* Leiden University